Jianzhu Dong
Key Laboratory of Dynamics
and Control of Flight Vehicle,
Ministry of Education and School
of Aerospace Engineering,
Beijing Institute of Technology,
Beijing 100081, China

Yuchen Zhao
Key Laboratory of Dynamics
and Control of Flight Vehicle,
Ministry of Education and School
of Aerospace Engineering,
Beijing Institute of Technology,
Beijing 100081, China

Yong Cheng
Key Laboratory of Dynamics
and Control of Flight Vehicle,
Ministry of Education and School
of Aerospace Engineering,
Beijing Institute of Technology,
Beijing 100081, China

Xiaoming Zhou[1]
Key Laboratory of Dynamics
and Control of Flight Vehicle,
Ministry of Education and School
of Aerospace Engineering,
Beijing Institute of Technology,
Beijing 100081, China
e-mail: zhxming@bit.edu.cn

Underwater Acoustic Manipulation Using Solid Metamaterials With Broadband Anisotropic Density

A new type of all-solid metamaterial model with anisotropic density and fluid-like elasticity is proposed for controlling acoustic propagation in an underwater environment. The model consists of a regular hexagonal lattice as the host that defines the overall isotropic stiffness, in which all lattice beams have been sharpened at both ends to significantly diminish the shear resistance. The inclusion structure, which involves epoxy, rubber, and lead material constituents, is designed to attain a large density–anisotropy ratio in the broad frequency range. The wave-control capability of metamaterials is evaluated in terms of underwater acoustic stretching, shifting, and ground cloaking, which are generated by the transformation acoustic method. The decoupling design method was developed for the metamaterial microstructure using band-structure, effective-medium, and modal-field analyses. The acoustic performance of these metamaterial devices was finally verified with full-wave numerical simulations. Our study provides new insight into broadband underwater acoustic manipulation by all-solid anisotropic-density metamaterials.
[DOI: 10.1115/1.4041318]

1 Introduction

In the past decade, the transformation acoustic method has emerged as a highly effective tool for acoustic propagation manipulation. The precise control over wave trajectory has stimulated many new technological concepts (e.g., rendering an object acoustically invisible, imaging defects beyond the diffraction limit). Transformation acoustics rely on mediums with highly anisotropic properties, which play a vital role in both the bending of wave trajectory and nonreflection wave behavior. Anisotropic stiffness and mass density are requested in a pentamode-inertial material, which is the most general material model derived from transformation acoustics [1]. Acoustic manipulation is typically implemented on the basis of two reduced versions of pentamode-inertial materials. One version refers to pure pentamode material [2], which possesses anisotropic stiffness and isotropic density. To satisfy the static equilibrium equation, the characteristic stress tensor of pentamode materials must be divergence free and symmetric [1,2]. This limits the pentamode acoustic control to special scenarios, such as the cloaking of geometrically regular objects [3,4] and transformation under quasi-symmetric mapping [5]. Our study focuses on the other version, referred to as inertial transformation, which features acoustic materials with anisotropic density and isotropic stiffness. Inertial transformation materials always satisfy static equilibrium conditions; hence, they can be applied in the arbitrary regulation of acoustic trajectory.

The anisotropic inertial density is enabled by Newton's law of motion and has been practically realized by various types of structured metamaterials, such as an alternating layered fluid-solid composite, which can generate an anisotropic density that exhibits extremely weak dispersion [6–8]. The underlying physics is attributed to the discontinuity or sliding effect of particle tangential motion at the fluid–solid interface. As a result of the weak dispersion, the anisotropic density can be held nearly constant in a broad frequency range, making broadband acoustic control possible, which is highly desirable in practical engineering. These fluid–solid composites are often called acoustic metafluids and are particularly effective for airborne sound manipulation, including acoustic cloaking [9,10], subdiffraction limited acoustic detection [11,12], and the unprecedented wavefront modulation [13–15]. For water environments, the anisotropic metafluids should be designed in the same manner by immersing isolated solid microstructures in water [16]. Considering that the fluid phase is potentially impractical, it is replaced by soft solid materials with low shear stiffness. However, the presence of shear resistance was found to significantly decrease the density–anisotropy ratio [17], thereby weakening the sound control capability of waterborne metafluids. To resolve this issue, a new type of all-solid metamaterial model is proposed in this work, which is more suitable for underwater acoustic manipulation.

In terms of pure solid metamaterials, the anisotropic density has already been realized on the basis of the local-resonance effect [18–23]. However, because of resonance-induced strong dispersion, the anisotropic density of those solid metamaterials can be held nearly constant in the narrow frequency band. In addition, the shear modulus of these locally resonant solid metamaterials with anisotropic density [18–23] has not been made extremely

[1]Corresponding author.
Contributed by the Applied Mechanics Division of ASME for publication in the Journal of Applied Mechanics. Manuscript received July 3, 2018; final manuscript received August 23, 2018; published online September 14, 2018. Assoc. Editor: Yashashree Kulkarni.

small. Recently, authors proposed a new type of solid metamaterials that could overcome these two limitations [24]. The proposed metamaterials simultaneously possess anisotropic stiffness and inertial density, wherein the weakly dispersive anisotropic density has been achieved in the broad frequency range by employing the sliding-interface concept associated with fluid–solid composites. It is also important to note that the shear stiffness of the model can be substantially reduced. As a result, the model can be reduced to the pentamode-inertial acoustic material [24], which is the most general material derived from transformation acoustic theory. On the basis of our previous work, we develop a solid metamaterial model with broadband anisotropic density and fluid-like elasticity, which is more conductive to underwater acoustic manipulation. The model geometry of anisotropic-density metamaterials with exceptionally low shear stiffness values are reported in Sec. 2. In Sec. 3, the transformation acoustics method is revisited; then, three wave-controlling examples (i.e., acoustic stretching, shifting, and ground cloaking) were developed according to inertial transformation. The guidelines for designing metamaterial structures of these functional devices are generally discussed, and the acoustic performance of the device is verified with numerical simulations. Finally, conclusions are provided in Sec. 4.

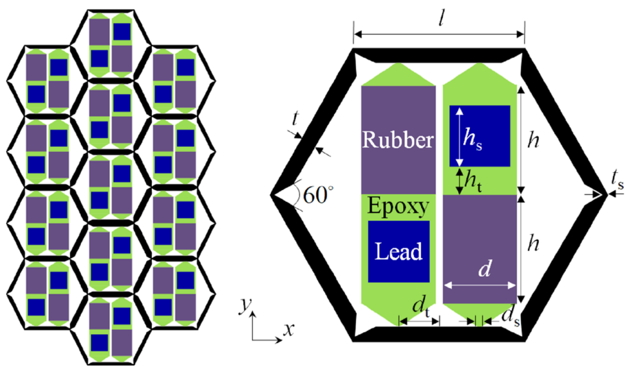

Fig. 1 The metamaterial model with broadband anisotropic density and fluid-like elasticity

2 Solid Metamaterials With Broadband Anisotropic Density and Fluid-Like Elasticity

2.1 Geometry of the Cell Model. Figure 1 shows a schematic of the metamaterial model with broadband anisotropic density and fluid-like elasticity. The host lattice consisted of a regular hexagonal cell that governed the overall isotropic stiffness, which can be modulated by the beam length l, the thickness t, and proper selection of the beam material. The ends of all strut beams were sharpened to achieve extremely small shear stiffness values, which gives the model its fluid-like elasticity [24]. Two bars sharing the same structures but deposited opposite one another were embedded inside the lattice, with sharpened ends that mimicked the sliding-boundary effect in fluid–solid composites for the broadband anisotropic density. In the left bar, the material directly connected to the lattice host was an epoxy with Young's modulus $E_Y = 4.35$ GPa, Poisson's ratio $v = 0.37$, and density $\rho = 1150\,\mathrm{kg/m^3}$, which served as a rigid connection to ensure uniform motion when the cell structure vibrated vertically. A lead plate ($E_Y = 40.8$ GPa, $v = 0.37$, and $\rho = 11600\,\mathrm{kg/m^3}$) was inserted into the bottom part of the epoxy to increase the total weight of the cell, whereas the partial epoxy on the top was replaced by soft rubber to diminish the resonant frequency of the model's horizontal vibration. The soft rubber structure also played an important role in weakening the dynamic coupling between the lattice host and inclusion, making it possible to modulate the overall stiffness without considering the effect of inclusion elasticity.

2.2 Effective-Medium Method. Figure 2(*c*) shows the typical band structure of the cell model, which inherits the dispersion characteristics of the dual-anisotropic metamaterials developed previously [24]. Both longitudinal (L) and transverse (T) wave modes on two perpendicular principle directions (i.e., horizontal ΓX and vertical ΓY) can be observed. A low-frequency bandgap, which arose because of the resonance of inclusion structures, disrupted the L branch on ΓX and T branch on ΓY. We previously discovered that this resonant gap is critical to the transition from isotropic density of the host lattice to broadband anisotropic density of the metasolid situated above the gap. To quantify the effective parameters of the metamaterial model, the effective-medium method, which was developed previously for the dual-anisotropic

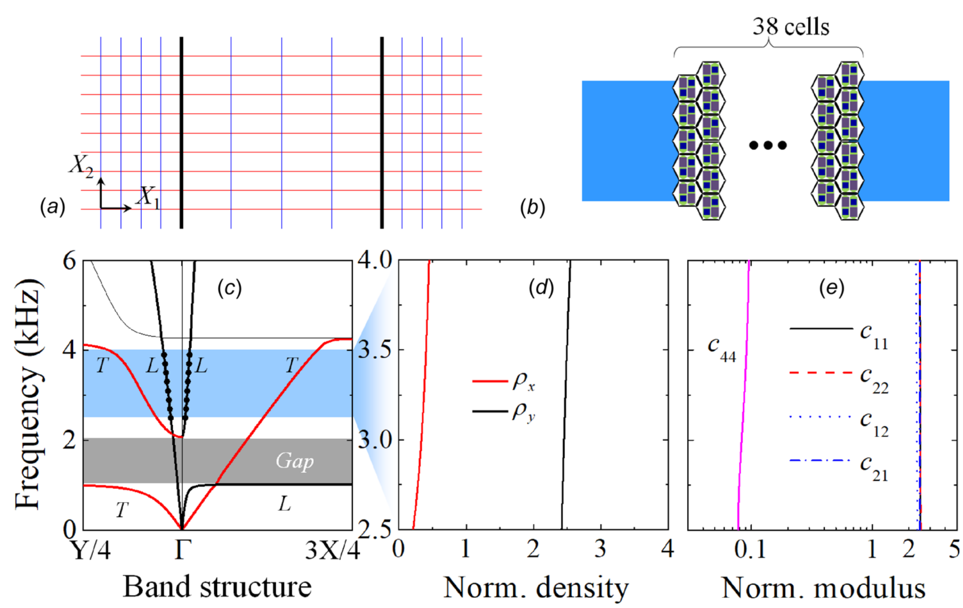

Fig. 2 (*a*) Coordinate grid of the stretching transformation and (*b*) schematic profile of the wave-stretching device assembled by metamaterial cells; (*c*) band diagrams, (*d*) effective densities, and (*e*) effective stiffness parameters of the wave-stretching metamaterials

metamaterial, was used. Recall that the constitutive equation governing the orthotropic elasticity is given by [24]

$$\begin{bmatrix} \sigma_{xx} \\ \sigma_{yy} \\ \sigma_{xy} \end{bmatrix} = \begin{bmatrix} c_{11} & c_{12} & 0 \\ c_{21} & c_{22} & 0 \\ 0 & 0 & c_{44} \end{bmatrix} \begin{bmatrix} \varepsilon_{xx} \\ \varepsilon_{yy} \\ 2\varepsilon_{xy} \end{bmatrix} \tag{1}$$

where the average stress and strain fields, $\sigma_{\alpha\beta}$ and $\varepsilon_{\alpha\beta}$ (α, $\beta = x$ or y), can be obtained from local field integrations over a single cell based on the band structure results [25]. The average normal stress and normal strain are obtained from the L modes, and the four elastic constants c_{11}, c_{12}, c_{21}, and c_{22} are determined according to $[\bar{\sigma}_{xx}, \bar{\sigma}_{yy}]_{\rm LX} = [(c_{11}, c_{12}), (c_{21}, c_{22})][\bar{\varepsilon}_{xx}, \bar{\varepsilon}_{yy}]_{\rm LX}$ and $[\bar{\sigma}_{xx}, \bar{\sigma}_{yy}]_{\rm LY} = [(c_{11}, c_{12}), (c_{21}, c_{22})][\bar{\varepsilon}_{xx}, \bar{\varepsilon}_{yy}]_{\rm LY}$. Average shear stress and shear strain are retrieved from the T modes. The shear stiffness c_{44} is then computed by either $(\bar{\sigma}_{xy})_{\rm TX} = c_{44}(2\bar{\varepsilon}_{xy})_{\rm TX}$ or $(\bar{\sigma}_{yx})_{\rm TY} = c_{44}(2\bar{\varepsilon}_{yx})_{\rm TY}$. The equation of inertial motion pertaining to the anisotropic density is expressed as

$$\begin{bmatrix} F_x \\ F_y \end{bmatrix} = -\omega^2 V \begin{bmatrix} \rho_x & 0 \\ 0 & \rho_y \end{bmatrix} \begin{bmatrix} u_x \\ u_y \end{bmatrix} \tag{2}$$

where the net force F_α and average displacement u_α are defined from the L modes [25], and V is the cell area. The density components are computed by $\rho_x = (-1/\omega^2 V)(F_x)_{\rm LX}/(\bar{u}_x)_{\rm LX}$ and $\rho_y = (-1/\omega^2 V)(F_y)_{\rm LY}/(\bar{u}_y)_{\rm LY}$. Using the effective-medium method, the optimal design for cell structures can be obtained, which will be explained below in terms of wave-controlling examples.

3 Underwater Acoustic Manipulation Based on Inertial Transformation

3.1 Revisit of Transformation Acoustics Method. The acoustic equation for homogeneous fluids is expressed as

$$\kappa_0 \nabla \cdot (\rho_0^{-1} \nabla p) - \ddot{p} = 0 \tag{3}$$

where κ_0 is the bulk modulus and ρ_0 is the mass density. Under arbitrary coordinate transformation from $\boldsymbol{X}$ to $\boldsymbol{x}$, Eq. (3) is transformed to the more general formulation called the pentamode-inertial equation [1]

$$\kappa \boldsymbol{S} : \nabla[\boldsymbol{\rho}^{-1} \nabla \cdot (\boldsymbol{S} p)] - \ddot{p} = 0 \tag{4}$$

where the pseudo-pressure p is defined as $p = -\kappa \mathrm{tr}(\boldsymbol{S}\boldsymbol{\varepsilon})$, in which $\boldsymbol{\varepsilon}$ is the strain tensor. $\boldsymbol{S}$ is the symmetric characteristic stress tensor of pentamode materials, which must satisfy the static equilibrium condition $\nabla \cdot \boldsymbol{S} = 0$. Two reduced versions of Eq. (4) are commonly employed for acoustic-path manipulation. One version is called the pure pentamode transformation, which sets the isotropic density $\boldsymbol{\rho} = \rho \boldsymbol{I}$. In this scenario, acoustic trajectory control relies on the anisotropic stiffness, conditioned on $\nabla \cdot \boldsymbol{S} = 0$. The other version refers to the inertial transformation, in which $\boldsymbol{S}$ is chosen as the identity tensor (i.e., $\boldsymbol{S} = \boldsymbol{I}$), so that $\nabla \cdot \boldsymbol{S} = 0$ can always be satisfied. Then, Eq. (4) can be reduced to

$$\kappa \nabla \cdot (\boldsymbol{\rho}^{-1} \nabla p) - \ddot{p} = 0 \tag{5}$$

where the density tensor $\boldsymbol{\rho}$ and bulk modulus κ of transformation mediums are given by [1,26]

$$\boldsymbol{\rho}^{-1} = \boldsymbol{A} \rho_0^{-1} \boldsymbol{A}^{\rm T} / \det \boldsymbol{A} \tag{6}$$

$$\kappa = \kappa_0 \det \boldsymbol{A} \tag{7}$$

where $\boldsymbol{A}$ is the Jacobian transformation tensor with components $A_{ij} = \partial x_i / \partial X_j$. Sections 3.2, 3.3, and 3.4 consider underwater acoustic stretching, shifting, and ground cloaking as examples, which are generated from the inertial transformations (6) and (7), to show how the desired material parameters can be practically realized by the proposed models with the help of the band-structure and effective-medium analyses.

Table 1 Geometric parameters of cell models

	Unit (mm)	Acoustic stretching	Acoustic shifting	Acoustic cloaking
Host strut	l	10.00		
	t	0.78	0.70	0.75
	t_s	0.45	0.40	0.43
Inclusion	h	5.70	5.50	6.00
	h_s	4.25	4.00	3.70
	h_t	0.73	0.75	1.15
	d	5.26	5.26	4.55
	d_s	0.11	0.11	0.09
	d_t	2.89	2.89	2.50

3.2 Acoustic Stretching. Consider the following coordinate transformation, which dictates the acoustic stretching

$$x_1 = \alpha X_1, \; x_2 = X_2 \tag{8}$$

Equations (6) and (7) therefore result in

$$[\boldsymbol{\rho}] = \rho_0 \begin{bmatrix} 1/\alpha & 0 \\ 0 & \alpha \end{bmatrix}, \quad \kappa = \kappa_0 \alpha \tag{9}$$

Figure 2(*a*) shows a schematic of the coordinate grids of the transformed space layer immersed in the background, with $\alpha = 2.5$. The material parameters to be realized can be expressed as

$$\rho_{11} = 0.4\rho_0, \quad \rho_{22} = 2.5\rho_0, \quad \kappa = 2.5\kappa_0 \tag{10}$$

where ρ_0 and κ_0 are set as $1000\,\mathrm{kg/m^3}$ and 2.25 GPa for water, respectively.

Figure 2(*c*) shows the plot of the band structure in the designed cell, which exhibits nearly linear dispersion in the broad frequency range ~2.5–4.0 kHz. The effective density and stiffness in this linear dispersion regime are shown in Figs. 2(*d*) and 2(*e*), respectively, matching very well with the objection parameters (10). Using these effective parameters and the dispersion equation $k_x^2/\rho_x + k_y^2/\rho_y = \omega^2/\kappa$, the dispersion curves of the effective medium have been calculated, as depicted by the solid circles in Fig. 2(*c*). The excellent agreement between the calculations and the band structure of the actual metamaterial verified the effective-medium assumption. Note that the optimized material parameters were $E_{\rm Y} = 15$ MPa, $\nu = 0.49$, and $\rho = 1100\,\mathrm{kg/m^3}$ for the rubber, and $E_{\rm Y} = 125$ GPa, $\nu = 0.25$, and $\rho = 1550\,\mathrm{kg/m^3}$ for the lattice host. Geometric parameters are listed in Table 1.

Given the desired material parameters (10), finalizing the material properties and geometric sizes of microstructures is often complicated. However, in our model, the microstructural parameters can be readily determined by developing a decoupling design for the overall stiffness and density. As mentioned previously, the nearly constant anisotropic density occurs in the weakly dispersive region above the low-frequency gap and is dominantly influenced by the inclusion structure. To understand the effect of the inclusion, the mode shapes relevant to this linear dispersion regime were analyzed. Figure 3(*a*) shows the modal displacement of the LX branches at the specific frequency of 3.5 kHz. These results indicate that the heavy lead plate remains virtually motionless, whereas the rubber and epoxy materials vibrate in opposite directions. This suggests that the inclusion represents a minor contribution to the translational momentum in the horizontal direction. As a result, the component ρ_x is close to the weight of the

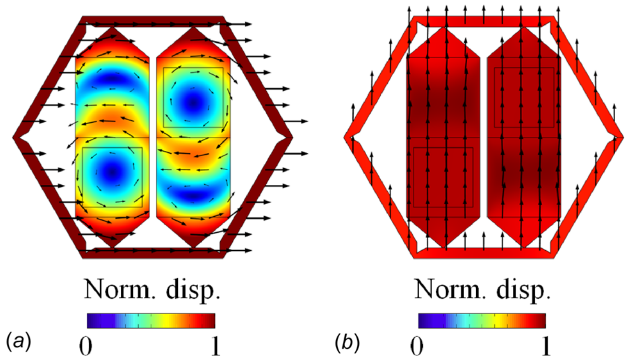

Fig. 3 The modal displacement fields of (*a*) LX and (*b*) LY branches in Fig. 2(*c*) at the frequency of 3.5 kHz

host lattice. Though given a minor influence on the horizontal momentum, the dynamic motion of the inclusion structure has a significant effect on the frequency range in which ρ_x is held nearly constant. The lower bound of the region was found to be right above the gap, and was caused by the lead-rubber resonance, whereas the upper bound refers to the frequency at which the LX band was interrupted by a nearly flat branch (Fig. 2(*c*)), which arose from the resonance of the rubber itself. The other density component ρ_y measures the total weight of the model [24], as evidenced by the LY mode shape in Fig. 3(*b*), in which the uniform motion of the entire cell can be observed.

The overall stiffness was governed by the host lattice. Figure 2(*e*) indicates that the shear stiffness c_{44} substantially decreased, with a value that was only 7% of the water modulus. In theory, the trivial c_{44} would lead to the same value of c_{11}, c_{12}, c_{21}, c_{22} for isotropic elasticity. Figure 2(*e*) depicts the retrieved stiffness parameters converging to the same value in the broad band ~2.5–4.0 kHz, which is also the bulk modulus κ. We then concluded that the overall elasticity was only slightly influenced by the inclusion, which induced the anisotropic stiffness. Note that the shear stiffness c_{44} was primarily dependent on the lattice beam connection thickness t_s. Figure 4 shows the average shear stiffness c_{44} over the band ~2.5–4.0 kHz for various t_s/t values. Shearing was decreased effectively by reducing t_s, whereas c_{11} was only slightly changed. Therefore, it is possible to modulate c_{44} by simply tuning the connection thickness t_s.

In summary, the decoupling design of the model allowed for the nearly independent modulation of any one parameter of κ, c_{44}, ρ_x, and ρ_y without affecting the others. The bulk modulus κ was only relevant to the cell beam rigidity and its slenderness ratio. The shear stiffness c_{44} can be minimized by reducing the beam

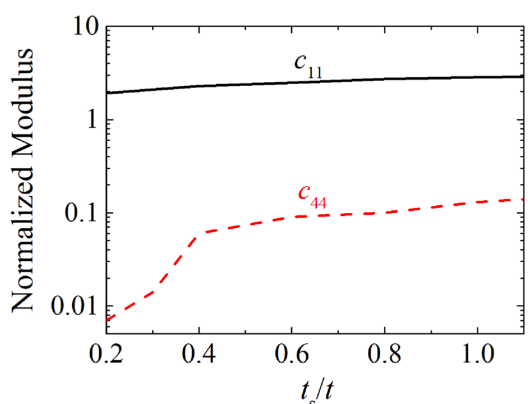

Fig. 4 The average shear stiffness c_{44} of the wave-stretching metamaterial over the frequency band ~2.5–4.0 kHz for various connection thickness t_s/t values

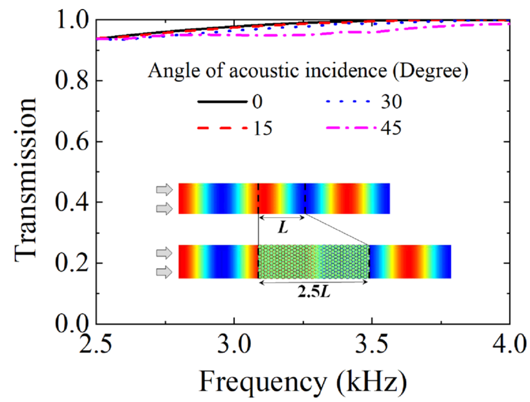

Fig. 5 Sound transmission spectrum of the wave-stretching metamaterial at incident angles of 0 deg, 15 deg, 30 deg, 45 deg. The pressure field distributions of sounds normally impacting the metamaterial at a frequency of 3.5 kHz are shown in the inset.

connection thickness t_s. The density component ρ_x was dependent on the weight of the host lattice, whereas ρ_y was the total weight of the entire cell, making it possible to enhance ρ_y by simply increasing the volume of lead. The frequency range of the linear dispersion, in which all effective parameters were held nearly constant, was bounded by the lead-rubber resonance as the lower limit and the rubber resonance itself as the upper limit. It is also important to note that the rubber had to be soft enough so that the effective stiffness remained unaffected by the inclusion structure.

Figure 2(*b*) shows the schematic of the acoustic-stretching device assembled by the designed metamaterial cell. Results of the finite element model were used to calculate underwater acoustic transmission of the device that was incident by plane waves of different incident angles 0 deg, 15 deg, 30 deg, and 45 deg as shown in Fig. 5. Nearly unity transmission was observed in the broad frequency band ~2.5–4.0 kHz, which verified the reflectionless nature of transformation mediums. The pressure distributions of sounds that normally impacted the wave-stretching material at a frequency of 3.5 kHz are illustrated in the inset. The pressure field distribution in the background water is also depicted in the figure for comparison. When the water of length L was replaced with the wave-stretching metamaterial that occupied a longer region 2.5L, the phase differences between input and output sides were exactly the same for the water and metamaterial. In other words, the travel time of the incident wave across the water and the metamaterial was the same. The result coincided excellently with the prescribed factor $\alpha = 2.5$ in the wave-stretching transformation.

3.3 Acoustic Shifting. In the previous wave-stretching example, the grid lines in the transformed coordinate remained perpendicular, and they were aligned with the background grid lines. Here, we introduce the concept of grid shifting along the X_2 direction, which is characterized by the factor β. The resultant transformation becomes

$$x_1 = \alpha X_1, \quad x_2 = X_2 + \beta X_1 \tag{11}$$

This shifting transformation forms an angle between the principle directions of the transformed and background space. According to Eqs. (6) and (7), material parameters in the transformed region can be expressed as

$$[\boldsymbol{\rho}] = \rho_0 \begin{bmatrix} \dfrac{1+\beta^2}{\alpha} & -\beta \\ -\beta & \alpha \end{bmatrix}, \quad \kappa = \kappa_0 \alpha \tag{12}$$

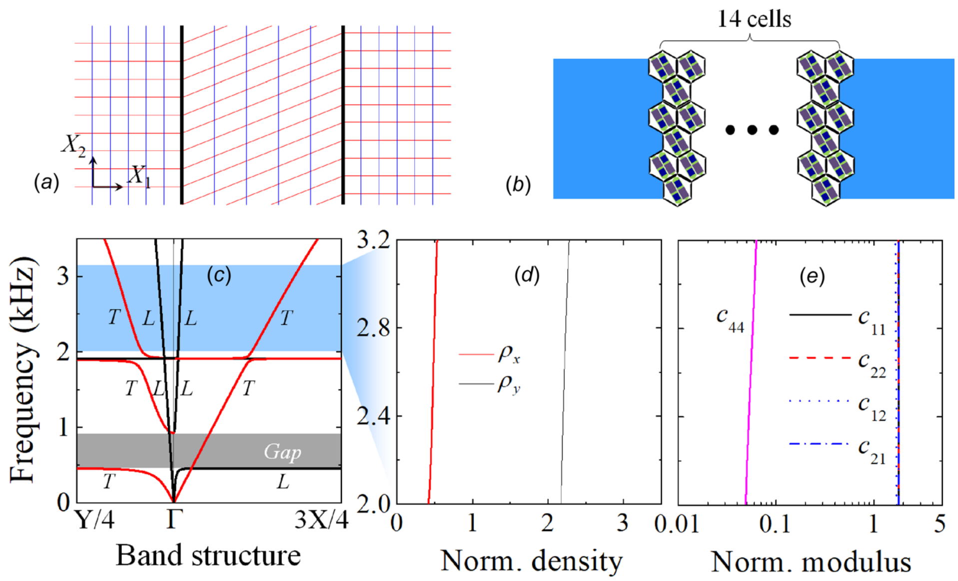

Fig. 6 Acoustic-shifting transformation results, which are similar to those in Fig. 2

The density matrix is written in the diagonal-component form as

$$[\boldsymbol{\rho}]^{\mathrm{pr}} = \rho_0 \mathrm{diag}\left[F_1 - \sqrt{F_1^2 - 1} \quad F_1 + \sqrt{F_1^2 - 1}\right] \tag{13}$$

with the principal angle θ given by

$$\theta = \arcsin\left(\frac{G_1}{\sqrt{1 + G_1^2}}\right) \tag{14}$$

where

$$F_1 = \frac{\alpha^2 + \beta^2 + 1}{2\alpha} \tag{15}$$

$$G_1 = \frac{\beta}{\alpha - F_1 + \sqrt{F_1^2 - 1}} \tag{16}$$

Set $\theta = 30$ deg in our illustrative example (Fig. 6(*a*)). A schematic of the assembled metamaterial device is shown in Fig. 6(*b*), with all model cells rotated counterclockwise by angle $\theta = 30$ deg. Assuming a stretching factor $\alpha = 1.8$, we have $\beta = 0.783$. The material parameters to be realized can be expressed as

$$\rho_{11}^{\mathrm{pr}} = 0.444\rho_0, \quad \rho_{22}^{\mathrm{pr}} = 2.252\rho_0, \quad \kappa = 1.8\kappa_0 \tag{17}$$

Figure 6(*c*) provides the band diagram of the cell structure designed as the building block of the acoustic-shifting material. Using the decoupling design strategy, the optimized material parameters were $E_{\mathrm{Y}} = 2$ MPa, $v = 0.49$, and $\rho = 870\,\mathrm{kg/m^3}$ for the rubber, and $E_{\mathrm{Y}} = 92$ GPa, $v = 0.35$, and $\rho = 1700\,\mathrm{kg/m^3}$ for the lattice host. Geometric parameters are listed in Table 1. Figures 6(*d*) and 6(*e*) show the effective density and stiffness of the model in the band ~2.0–3.2 kHz, which met the requirement in Eq. (17). In contrast to the previous example, where the operating band located immediately above the low-frequency gap created by the rubber-lead resonance, the frequency band of operation in this example was chosen in the region beyond the relatively flat branch near 1.91 kHz. Figure 7 depicts the plot of the modal displacement at 2.5 kHz, which clearly disclosed the anisotropic-inertial effect within this regime. The flat dispersion was attributed to the rubber resonance itself. As a result, the momentum contribution from the inclusion is still minor when the cell

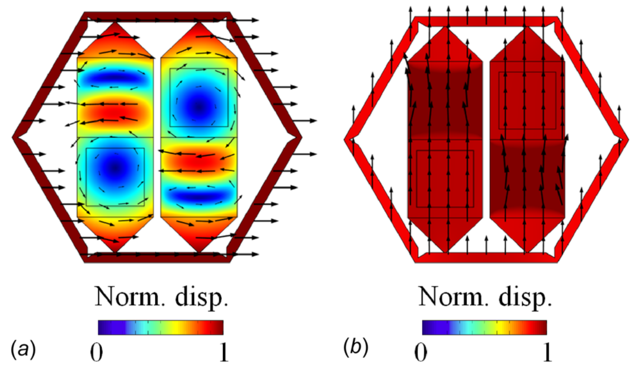

Fig. 7 The modal displacement fields of (*a*) LX and (*b*) LY branches in Fig. 6(*c*) at a frequency of 2.5 kHz

structure oscillates horizontally. The uniform motion in the vertical direction was again achieved. Our results demonstrated the flexible optimization of the models, which realized broadband anisotropic density in the frequency band either beyond or below the flat branch related to the rubber resonance.

Figure 8(*a*) shows the pressure field distribution produced by a line source (operating at 3.0 kHz) placed on the left side of the homogeneous material with ideal parameters (17). The incident beam clearly shifted upward with the prescribed factor $\beta = 0.783$ after passing the wave-shifting material. Figure 8(*b*) shows the corresponding results for the assembled cell structure that replaced the homogeneous version, in which the remarkably similar acoustic-shifting phenomenon was observed.

3.4 Acoustic Ground Cloaking. As a final example, the design of acoustic ground cloak conceived previously by Popa and Cummer [16] was implemented. As shown schematically in Fig. 9(*a*), the ground cloak was formed by the following linear coordinate transformation:

$$x_1 = X_1, \quad x_2 = \frac{c}{c - a}\left(-a + \frac{a}{b}|X_1| + X_2\right) \tag{18}$$

The density matrix is written in the principle coordinate system as [16]

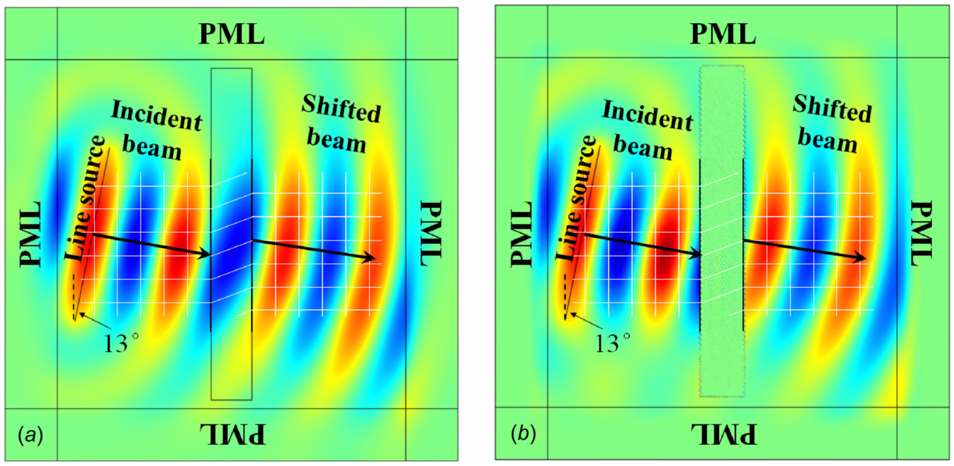

Fig. 8 Pressure field distributions produced by a line source of operating frequency of 3.0 kHz, placed on the left side of (*a*) the ideal homogeneous wave-shifting material and (*b*) the structured metamaterial device

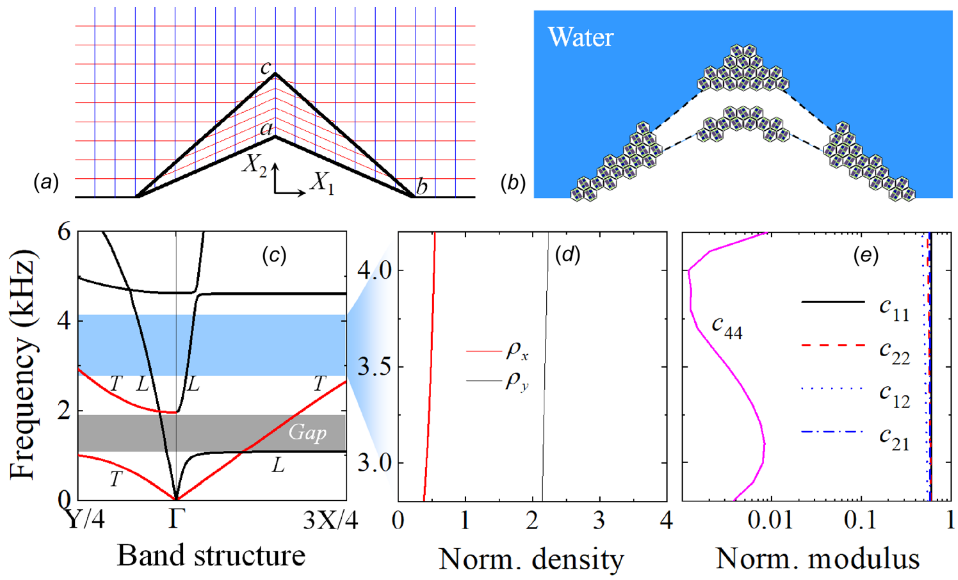

Fig. 9 Acoustic ground cloaking transformation results, which are similar to those in Fig. 2

$$[\boldsymbol{\rho}]^{\mathrm{pr}} = \rho_0 \mathrm{diag}\left[F_2 - \sqrt{F_2^2 - 1} \quad F_2 + \sqrt{F_2^2 - 1}\right] \tag{19}$$

with the principal angle θ given by

$$\theta = \mathrm{sign}(X_1)\arcsin\left(\frac{G_2}{\sqrt{1+G_2^2}}\right) \tag{20}$$

where

$$F_2 = 1 + \frac{a^2(b^2+c^2)}{2b^2c(c-a)} \tag{21}$$

$$G_2 = \frac{b}{c}\left[1 - \frac{c-a}{a}\left(F_2 - 1 + \sqrt{F_2^2 - 1}\right)\right] \tag{22}$$

The bulk modulus is [16]

$$\kappa = \kappa_0(c-a)/c \tag{23}$$

Consider geometric parameters $a = 43$ cm, $b = 100$ cm, and $c = 100$ cm. The required densities and bulk modulus are

$$\rho_{11}^{\mathrm{pr}} = 0.46\rho_0, \quad \rho_{22}^{\mathrm{pr}} = 2.172\rho_0, \quad \kappa = 0.58\kappa_0 \tag{24}$$

The principal angle is $\theta \approx 30$ deg for the left region ($X_1 < 0$) and $\theta \approx -30$ deg for the right region ($X_1 > 0$). Equation (24) means that one needs to design only one type of element cells, which are assembled symmetrically with respect to the central vertical line, as depicted schematically in Fig. 9(*b*). Following the decoupling design strategy generalized previously, we optimized the cell structures, obtaining material parameters $E_{\mathrm{Y}} = 20$ MPa, $\nu = 0.49$, and $\rho = 1150\,\mathrm{kg/m^3}$ for the rubber, and $E_{\mathrm{Y}} = 30$ GPa, $\nu = 0.3$, and $\rho = 2500\,\mathrm{kg/m^3}$ for the lattice host. Geometric parameters are listed in Table 1. The band structure of the unit cell is presented in Fig. 9(*c*), which depicts the nearly linear dispersion at frequencies ~2.8–4.2 kHz. Effective parameters in this frequency range were retrieved as shown in Figs. 9(*d*) and 9(*e*), and were found to match quite well with the cloaking parameters (24).

Figure 10 shows the simulation results of the acoustic performance of the ground cloak. The ideal ground-reflection case is illustrated in Fig. 10(*a*), where a Gaussian beam operating at 3.0 kHz is incident at an angle 45 deg on the ground plane. The simulated pressure field distribution revealed that acoustic beam was completely reflected toward the right side. When a rigid triangular

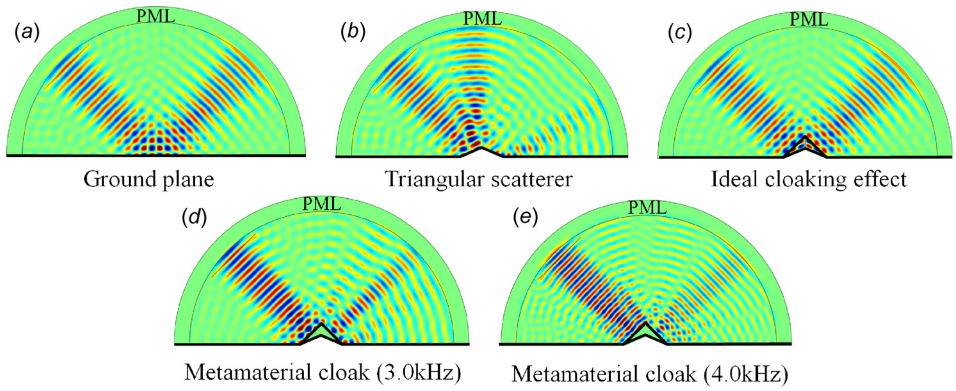

Fig. 10 Simulated pressure field distributions of a Gaussian beam operating at 3.0 kHz and incident at an angle of 45 deg on (*a*) the ground plane, (*b*) the rigid triangular object on the ground, and (*c*) the object covered by the ideal homogeneous cloak. Acoustic performance simulation results of the metamaterial ground cloaking device at frequencies (*d*) 3.0 kHz and (*e*) 4.0 kHz.

scatterer was placed above the ground, the incident beam was scattered in various random directions, making the object detectable, as illustrated in Fig. 10(*b*). The pressure distribution becomes identical to that of the ideal ground reflection when the object was covered by the homogeneous cloak with material parameters (24) (Fig. 10(*c*)). Figure 10(*d*) gives the simulation results of the metamaterial cloak, exhibiting ground-reflection performance that was similar to that of the ideal cloak in Fig. 10(*c*). This good match can be also observed at other operating frequencies (e.g., at 4.0 kHz), as shown in Fig. 10(*e*).

By exploring numerical examples of acoustic stretching, shifting, and ground cloaking transformations, we verified the broadband anisotropic density and fluid-like elasticity of the proposed metamaterials while also clearly demonstrating their ability to control acoustic propagation trajectories in the water environment. The decoupling strategy was proposed to allow for the easy microstructure design of the cell models. The optimized models contained materials that were all practically attainable, and experimental implementation can thus be expected. The proposed model may open a new route toward acoustic propagation control based on inertial transformation.

4 Conclusions

In our previous research [24], we developed a new type of elastic metamaterial with broadband anisotropic density, which was achieved by mimicking the sliding-interface concept in fluid–solid composites. We also found that extremely small shear stiffness values could be realized, which gave the model its fluid-like elasticity. These findings motivate us to develop a new material platform for underwater acoustic manipulation based on transformation acoustic method. In contrast to the previous model, this significant improvement, especially for the inclusion structure, resulted in a large density-anisotropy ratio. In addition, the improved model follows the decoupling design strategy, which provides the flexible and efficient optimization of microstructural parameters. Namely, the decoupling design of the model allows for the nearly independent modulation of any one parameter of κ, c_{44}, ρ_x, and ρ_y without influencing the others. Using underwater acoustic stretching, shifting, and ground cloaking as examples, we described the wave signature in detail and microstructure design of cell models using band-structure, effective-medium, and modal-field analyses. These metamaterial devices were then verified by full-wave numerical simulations. Results of our study suggest that the proposed model is a viable approach to the practical realization of underwater acoustic manipulation.

Funding Data

- 111 project (B16003).
- National Natural Science Foundation of China (11521062, 11572039, and 11622215).

References

[1] Norris, A. N., 2008, "Acoustic Cloaking Theory," Proc. R. Soc. London Ser. A, **464**(2097), pp. 2411–2434.
[2] Milton, G. W., and Cherkaev, A. V., 1995, "Which Elasticity Tensors Are Realizable?," ASME J. Eng. Mater. Technol., **117**(4), pp. 483–493.
[3] Chen, Y., Liu, X., and Hu, G., 2015, "Latticed Pentamode Acoustic Cloak," Sci. Rep., **5**, p. 15745.
[4] Chen, Y., Zheng, M., Liu, X., Bi, Y., Sun, Z., Xiang, P., Yang, J., and Hu, G., 2017, "Broadband Solid Cloak for Underwater Acoustics," Phys. Rev. B, **95**(18), p. 180104.
[5] Chen, Y., Liu, X., and Hu, G., 2016, "Design of Arbitrary Shaped Pentamode Acoustic Cloak Based on Quasi-Symmetric Mapping Gradient Algorithm," J. Acoust. Soc. Am., **140**(5), pp. EL405–EL409.
[6] Daniel, T., and José, S.-D., 2008, "Anisotropic Mass Density by Two-Dimensional Acoustic Metamaterials," New J. Phys., **10**(2), p. 023004.
[7] Zigoneanu, L., Popa, B.-I., Starr, A. F., and Cummer, S. A., 2011, "Design and Measurements of a Broadband Two-Dimensional Acoustic Metamaterial With Anisotropic Effective Mass Density," J. Appl. Phys, **109**(5), p. 054906.
[8] Qiu, C., Hao, R., Li, F., Xu, S., and Liu, Z., 2012, "Broadband Transmission Enhancement of Acoustic Waves Through a Hybrid Grating," Appl. Phys. Lett., **100**(19), p. 667.
[9] Zigoneanu, L., Popa, B.-I., and Cummer, S. A., 2014, "Three-Dimensional Broadband Omnidirectional Acoustic Ground Cloak," Nat. Mater, **13**(4), pp. 352–355.
[10] Popa, B.-I., Zigoneanu, L., and Cummer, S. A., 2011, "Experimental Acoustic Ground Cloak in Air," Phys. Rev. Lett., **106**(25), p. 253901.
[11] Liu, F., Cai, F., Peng, S., Hao, R., Ke, M., and Liu, Z., 2009, "Parallel Acoustic Near-Field Microscope: A Steel Slab With a Periodic Array of Slits," Phys. Rev. E, **80**(2 Pt 2), p. 026603.
[12] Zhu, J., Christensen, J., Jung, J., Martin-Moreno, L., Yin, X., Fok, L., Zhang, X., and Garcia-Vidal, F. J., 2011, "A Holey-Structured Metamaterial for Acoustic Deep-Subwavelength Imaging," Nat. Phys., **7**(1), pp. 52–55.
[13] Li, Y., Liang, B., Gu, Z., Zou, X., and Cheng, J., 2013, "Reflected Wavefront Manipulation Based on Ultrathin Planar Acoustic Metasurfaces," Sci. Rep., **3**(1), p. 2546.
[14] Tang, K., Qiu, C., Ke, M., Lu, J., Ye, Y., and Liu, Z., 2014, "Anomalous Refraction of Airborne Sound Through Ultrathin Metasurfaces," Sci. Rep., **4**(1), p. 6517.
[15] Xie, Y., Wang, W., Chen, H., Konneker, A., Popa, B.-I., and Cummer, S. A., 2014, "Wavefront Modulation and Subwavelength Diffractive Acoustics With an Acoustic Metasurface," Nat. Commun., **5**(1), p. 5553.
[16] Popa, B.-I., and Cummer, S. A., 2011, "Homogeneous and Compact Acoustic Ground Cloaks," Phys. Rev. B, **83**(22), p. 224304.
[17] Popa, B.-I., Wang, W., Konneker, A., Cummer, S. A., Rohde, C. A., Martin, T. P., Orris, G. J., and Guild, M. D., 2016, "Anisotropic Acoustic Metafluid for Underwater Operation," J. Acoust. Soc. Am., **139**(6), pp. 3325–3331.
[18] Milton, G. W., and Willis, J. R., 2007, "On Modifications of Newton's Second Law and Linear Continuum Elastodynamics," Proc. R. Soc. London Ser. A, **463**(2079), pp. 855–880.

[19] Huang, H. H., and Sun, C. T., 2011, "Locally Resonant Acoustic Metamaterials With 2D Anisotropic Effective Mass Density," Philos. Mag., **91**(6), pp. 981–996.
[20] Liu, A. P., Zhu, R., Liu, X. N., Hu, G. K., and Huang, G. L., 2012, "Multi-Displacement Microstructure Continuum Modeling of Anisotropic Elastic Metamaterials," Wave Motion, **49**(3), pp. 411–426.
[21] Zhu, R., Chen, Y. Y., Wang, Y. S., Hu, G. K., and Huang, G. L., 2016, "A Single-Phase Elastic Hyperbolic Metamaterial With Anisotropic Mass Density," J. Acoust. Soc. Am., **139**(6), pp. 3303–3310.
[22] Zhu, R., Huang, G. L., Huang, H. H., and Sun, C. T., 2011, "Experimental and Numerical Study of Guided Wave Propagation in a Thin Metamaterial Plate," Phys. Lett. A, **375**(30–31), pp. 2863–2867.
[23] Zhu, R., Liu, X. N., Huang, G. L., Huang, H. H., and Sun, C. T., 2012, "Microstructural Design and Experimental Validation of Elastic Metamaterial Plates With Anisotropic Mass Density," Phys. Rev. B, **86**(14), p. 144307.
[24] Cheng, Y., Zhou, X., and Hu, G., 2017, "Broadband Dual-Anisotropic Solid Metamaterials," Sci. Rep., **7**(1), p. 13197.
[25] Liu, X. N., Hu, G. K., Huang, G. L., and Sun, C. T., 2011, "An Elastic Metamaterial With Simultaneously Negative Mass Density and Bulk Modulus," Appl. Phys. Lett., **98**(25), p. 251907.
[26] Chen, H., and Chan, C. T., 2007, "Acoustic Cloaking in Three Dimensions Using Acoustic Metamaterials," Appl. Phys. Lett., **91**(18), p. 183518.